Disclosing recurrence properties in fluidized beds

F. Dabbagh [1,*] S. Pirker [2,†] T. Lichtenegger [2,‡] and S. Schneiderbauer [1,2,§]

[1] *Christian Doppler Laboratory for Multi-Scale Modeling of Multiphase Processes, Johannes Kepler University, Altenbergerstraße 69, 4040 Linz, Austria*

[2] *Department of Particulate Flow Modelling, Johannes Kepler University, Altenbergerstraße 69, 4040 Linz, Austria*

(Received 10 November 2020; accepted 2 April 2021; published 23 April 2021)

In this paper we shortly investigate the similarity between states for different fluidized bed regimes, which is an essential requirement for the application of recurrence computational fluid dynamics (rCFD) [Lichtenegger and Pirker, Chem. Eng. Sci. **153**, 394 (2016)]. Therefore, bubbling and turbulent fluidization regimes are outlined in the frame of different variable-based recurrence/distance norms (rNorm/dNorm). This last is typically used to quantify the degree of flow similarity within the observation time span. The recurrence plots or the so-called recurrence/distance matrices are accordingly constructed upon the rNorm/dNorm values and show no recurrence tendency for the full-resolved turbulent fluidization regimes. It is reported thereabouts that the high fluctuated nature of turbulent fluidization (interphase small scales) absentees the periodicity, and a disclosing procedure for the superstructure (large-scale) dynamics is vitally needed. To that end, a spatial filtering with the idea of the domain decomposition (recurrence island) has been applied to reveal a proper posterior indicator of turbulent fluidization recurrence. The filtering approach handles in increasing the recurrence prominence without changing the system behavior and makes the recurrence more visible. From other perspectives, a turbulence modeling using the coarse-grained approximate deconvolution model–two-fluid model (ADM-TFM) is employed for the turbulent fluidization case. Following its recurrence investigations, the resultant prominence offered by ADM-TFM is in a very comparable aspect to the same grid spatial filtering.

DOI: 10.1103/PhysRevFluids.6.044310

I. INTRODUCTION

Fluidization is an operation by which a set of solid particles is suspended in blowing gas or liquid upwards and moves like high viscous liquid behavior. This allows a worthwhile contacting process leading to conscientious mixing and favorable heat and mass transfer properties. One of the eminent examples thereof are the fluidized bed (FB) reactors [1]. They are classified as attractive tools for chemical processing industries with prominent applications in coating, granulation, coking, drying, and synthesis of fuels and polymers. Nonetheless, due to variety of the gas-solid interacting scales, most of the fluidized bed numerical models are limited to an expensive short duration. In the light of this shortcoming, our group have recently introduced the concept of recurrence computational fluid dynamics (rCFD) for the time-efficient modeling of pseudoperiodic flows [2]. Therewith, the

*firas.dabbagh@jku.at
†stefan.pirker@jku.at
‡thomas.lichtenegger@jku.at
§simon.schneiderbauer@jku.at

similarity between states, e.g., (t, t'), separated by a recurrence time step Δt_{rec}, is quantified by means of a distance (dNorm) $D^{\varphi}_{t,t'}$ or recurrence (rNorm) $R^{\varphi}(t, t')$ [2] norm, given by

$$D^{\varphi}_{t,t'} = \frac{\int d^3x[\varphi(t) - \varphi(t')]^2}{\max \int d^3x[\varphi(t) - \varphi(t')]^2}, \quad \text{and} \quad R^{\varphi}(t, t') = 1 - D^{\varphi}_{t,t'}, \tag{1}$$

where φ is chosen depending on the phenomenon of interest. The rNorm (R^{φ}) is interpreted as a degree of recurrence relative to the most extreme distinctness (D^{φ}) of occurring states. Equation (1) generalizes the original definition given in Ref. [3], which delineates a binary or thresholded recurrence [$R(t, t') \in \{0, 1\}$]. Namely, first, Eq. (1) allows continuous extents of similarity, which are referred to as unthresholded recurrence matrices [4]. Second, Eq. (1) contains information from the whole flow field at each moment t, which is different than the most experimental studies that process signals from single point probes to determine $R(t, t')$ [5,6]. On top of a sequence of rNorm values a recurrence plot is constructed to be used afterwards for an extended path prediction [2]. We call the recurrence plot as a recurrence matrix (rMatrix) $R^{\varphi}_{n,m}$ [7], similar to a distance matrix (dMatrix) $D^{\varphi}_{n,m}$, defined as

$$D^{\varphi}_{n,m} \equiv D^{\varphi}(n\,\Delta t_{\text{rec}}, m\,\Delta t_{\text{rec}}), \quad \text{and} \quad R^{\varphi}_{n,m} \equiv 1 - D^{\varphi}_{n,m}. \tag{2}$$

The off-diagonal entries with the lower values on the dMatrix indicate the field similarity between two instants, whereas the adequacy of dMatrix size (i.e., $n \equiv m$) can, in turn, be judged by computing the average degree of recurrence D^{φ}_{sim}. It renders the mean calculation of the (off-diagonal) most similar moments [8] inside the dMatrix and reads as

$$D^{\varphi}_{\text{sim}} = \frac{1}{N} \sum_{m}^{N} \min_n D^{\varphi}_{n,m}. \tag{3}$$

When the ongoing evolution of the mean starts to get insensitive to appending more states, the flow then can be considered repeated enough and the size of the dMatrix is sufficient. The concept of a recurrence plot had engrossed many authors as a visual tool to analyze the dynamical behavior of nonlinear systems [9]. For instance, it had been utilized for the cyclic events characterization in turbulent flows [10], the analysis of trailing-edge vortex shedding [11], on a velocity time series of magnetohydrodynamic turbulent channel flow [12], and for stochastic random dynamical systems [13]. Time-series data taken from single probes were usually processed to construct the recurrence plot in different than our global rCFD norm. In this scope fall furthermore various investigations on the hydrodynamics in fluidized beds using the recurrence plots as in Refs. [5,6,14–16]. The novel methodology of rCFD has been successfully applied for the fast modeling of long-term chemical species and heat propagation in bubbling FB reactors [7,17–19]. Therein, the bubble evolution was clearly identified with recurrent running, and the solid/gas volume fraction $\alpha_{s/g}$ was utilized as a variable-based φ in the rNorm computation.

In the present paper, we aim to shed light on the following research question: *Do the pure turbulent fluidization regimes actually have a kind of recurrent tendency?* To that end, we consider a series of instantaneous fields taken of bubbling and turbulent fluidized bed simulations where the two-fluid model (TFM) [20] is adopted. They have been investigated in the framework of evaluating the dNorm and dMatrix with the aim for disclosing its tendency to recurrent behavior. Therefore, in this paper, we abstain from presenting the details of the utilized TFM since our review is independent of the choice of the physical and numerical representations. Following that approach, the observations do not unveil a recurrent nature in the turbulent fluidization regimes, and posterior procedures are absolutely required to explore the periodicity of coherent uniform flows. The paper is arranged in a twofold aspect. One for bubbling FB in Sec. II, and the other for turbulent FB in Sec. III. At the end, conclusions are given in Sec. IV.

TABLE I. Summary of physical properties, principal flow conditions, and simulation parameters for the bubbling, full-resolved, and coarse-grained turbulent fluidized beds studied.

Property/condition	Symbol	Bubbling FB	Turbulent FB	ADM-TFM	Unit
Gas density	ρ_g		1.224		kg m^{-3}
Gas viscosity	μ_g		1.7894×10^{-5}		Pa s
Particle diameter	d_s		150×10^{-6}		m
Hexahedral grid size	$\Delta \boldsymbol{r}_i$	1.25×10^{-3}	1.22×10^{-3}	9.76×10^{-3}	m
Recurrence time step	Δt_{rec}	0.1	0.04		s
Initial solids inventory	m_{bed}	900	4500		gr
Particle density	ρ_s	860	2500		kg m^{-3}
Inlet fluidization velocity	$\|\boldsymbol{u}_{in}\|$	0.4	0.63		m s^{-1}
Width	W	0.01875	0.04		m
Length	L	0.14875	0.15		m
Height	H	0.39875	1.25		m

II. BUBBLING FLUIDIZED BED

We simulate a bubbling fluidized bed (Geldart's B group) using the Eulerian model of ANSYS FLUENT within the TFM framework [20]. The operating parameters and simulation details are given in Table I. After storing a series of sequences of the fields, separated by Δt_{rec}, the dMatrix is constructed on the base of the solid volume fraction D^{α_s} and solid fluxes $D^{\boldsymbol{\phi}_s}$, where $\boldsymbol{\phi}_s = \alpha_s \boldsymbol{u}_s$ as represented in Fig. 1. With a close inspection therein, one can note the analogous behavior of reoccurring patterns on α_s and $\boldsymbol{\phi}_s$ with lower dNorm values identified on the fluxes. The dMatrix in both can be characterized by regular long-term segments parallel to the diagonal to indicate similar events of solid distribution repeated after some time. In other words, line segments with 45° slopes, that run far from the diagonal by a certain distance, imply a uniform similarity between temporally separated states over a finite duration. In our case, the separation between segments is controlled by the corresponding frequency of coherent (mesoscopic) rising bubbles and their subsequent entrainment to the freeboard.

In general, the low-frequency macroscopic structures (coalescence and eruptions of large bubbles) together with the high-frequency microscopic structures (single particle-particle and fluid-particle interactions), determine the complex dynamics of fluidized beds [5]. Our dMatrix shows a

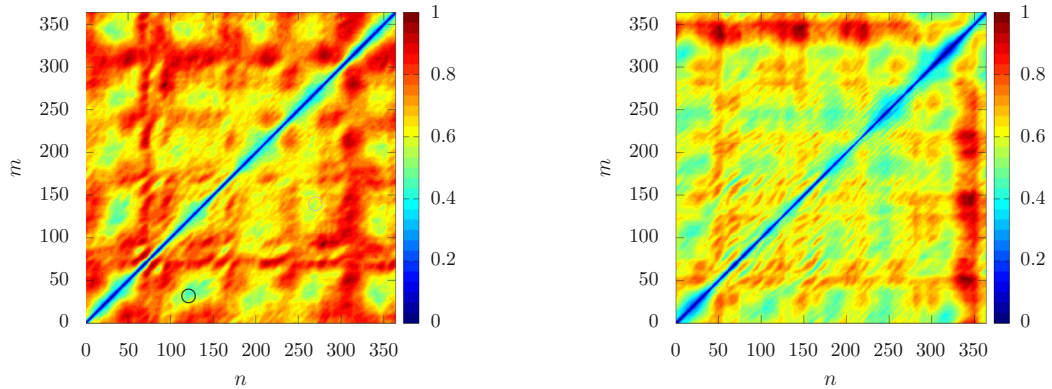

FIG. 1. The dMatrix of the dNorm (a) D^{α_s} and (b) $D^{\boldsymbol{\phi}_s}$ for the bubbling fluidized bed.

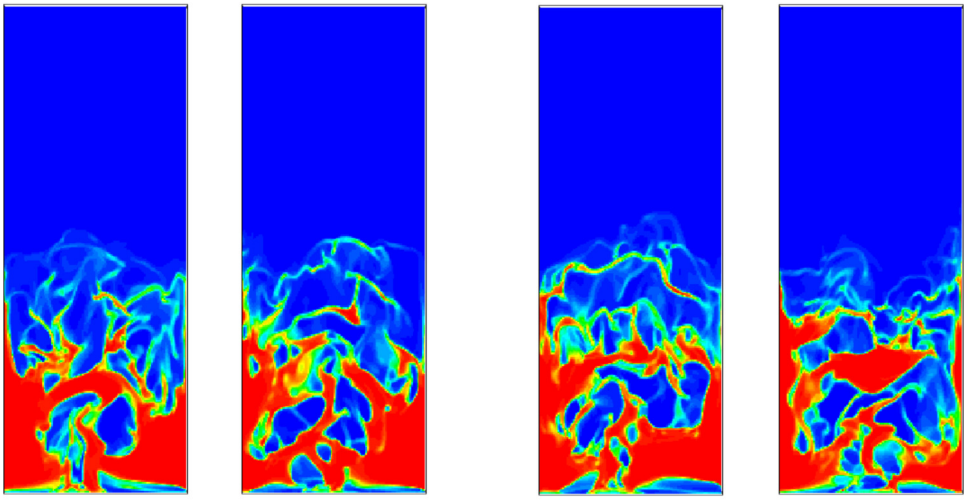

FIG. 2. Midwidth planes of α_s at two recurrence states, (a) $D_1^{\alpha_s}(121, 32) = 0.428$ [black circle in Fig. 1(a)], and (b) $D_2^{\alpha_s}(270, 140) = 0.52$ [white circle in Fig. 1(a)] in the bubbling fluidized bed.

short start phase, which is followed by repeated bubbling. The dynamics can be characterized by almost a pair of bubbles induced at the bottom and arise across the particles (see snaps in Fig. 2). The bubbles coalesce upwards to eventually either erupt on the bed surface or break up into smaller bubbles. These latter, then, moves downwards at the sides and bend again joining new rising bubbles. One can observe the evolution of such similar states by simply picturing α_s at a low dNorm value. For example, let us consider two pairs in Fig. 1(a) that correspond to $D_1^{\alpha_s}(121, 32) = 0.428$ (black circle) and $D_2^{\alpha_s}(270, 140) = 0.52$ (white circle). By plotting the midwidth plane of α_s in Figs. 2(a) and 2(b), respectively, we can note the high degree of similarity between the states which affords a clear signature on the system periodicity. Another quantitative property of recurrence can be in measuring the fluctuation amplitude of the so-called recurrence vector (rVector) [7]. That said, by drawing the values of the rNorm/dNorm along the horizontal line $m = \text{cte}$ on the rMatrix/dMatrix, the profile should fluctuate around a horizontal mean (recurrence plateau rPlateau) reaching a good variance, named as recurrence prominence rProminence. Thus, we generate the rVector profiles on the dMatrices in Figs. 1(a) and 1(b) at $m = 30$ and 20 and show them in Figs. 3(a) and 3(b), respectively. One can note the good rProminence presented by both dNorms for the current bubbling FB case.

Looking back to the dMatrices, the adequacy of matrix size is assessed by computing the ongoing mean parameter $D_{\text{sim}}^{\alpha_s}$, given in Eq. (3). It discloses the temporal mean accumulation of the (off-diagonal) most similar instants as depicted in Fig. 4(b). The profile, therein, unveils an initial increase towards a particular difference and, subsequently, saturated at a constant plateau after approximately $n = 100$. We interpret this behavior that the states start to reoccur after, at least, this time, with a degree of similarity of 0.5, and longer observations indicate similar reappearances to satisfy the sequence plenty. In order to get *local* insight on how the dynamics arranges in time (instead of the global background $D_{t,t'}^{\varphi}$), the magnitude of the solid flux gradient tensor is considered at each flow state. Therewith, we aim to expose the spatial correlation of multiscale dynamics along its history ($n \equiv m$). It is noteworthy to evoke the strong sensitivity of $\boldsymbol{\phi}_s$ to the uniform flow periodicity and rising bubbles passage [19]. Because of the high effective solid mixing persistent through the wake effect-particles, emulsion drift-particles, and the bubble eruptions-particles [21], the solid flow stands as a delicate feature for FB periodic structures and bubbles passage. Hence,

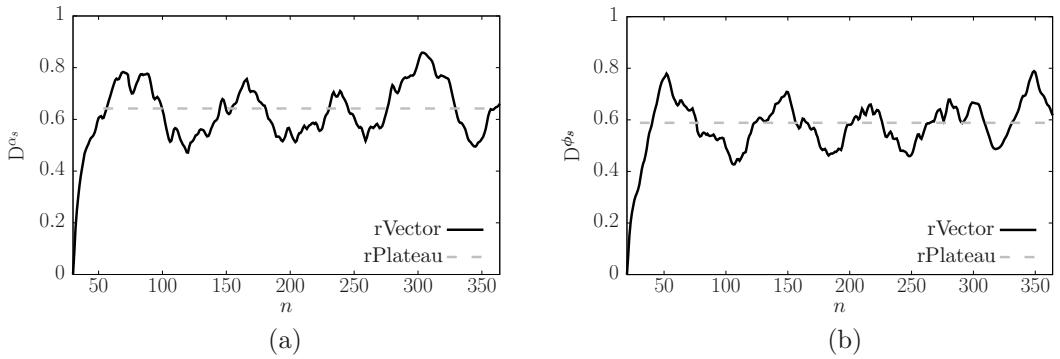

FIG. 3. The rVector profiles taken along the horizontal line $m = 30$ on (a) dMatrix D^{α_s} in Fig. 1(a) and $m = 20$ on (b) dMatrix D^{ϕ_s} in Fig. 1(b) in the bubbling fluidized bed.

we investigate the probability density function (PDF) of $\|\nabla \boldsymbol{\phi}_s\|$ at two unsimilar time segments, i.e., $n = 50$ and 100 and plot them in Fig. 4(a). Therein, the $\|\nabla \boldsymbol{\phi}_s\|$ data are represented on the logarithmic scale after an exponential bin width division. A clear no overlapping event is observed, particularly, in the lower ranges of $\|\nabla \boldsymbol{\phi}_s\|$, which correspond to the large-scale uniform flow. This indicates that the *local* large-scale structures are really uncorrelated in-between the periodic lags, whereas the small-scale structures rendered by high values of $\|\nabla \boldsymbol{\phi}_s\|$ are correlated because of fluctuations.

III. TURBULENT FLUIDIZED BED

We simulate a turbulent fluidized bed (Geldart's B group) using the TFM solver (TWOPHASEEULERFOAM) distributed with OPENFOAM 6. The operating parameters and simulation details are summarized in Table I [22]. Identically to the bubbling fluidized bed case, the dMatrix of the solid volume fraction D^{α_s} and solid fluxes D^{ϕ_s}, are constructed and displayed in Figs. 5(a) and 5(b), respectively. The dynamics in this regime follows an initial stage of disrupting the packed particles by the gas [Fig. 9(a)] isolating, straightforwardly, the posterior dynamics from

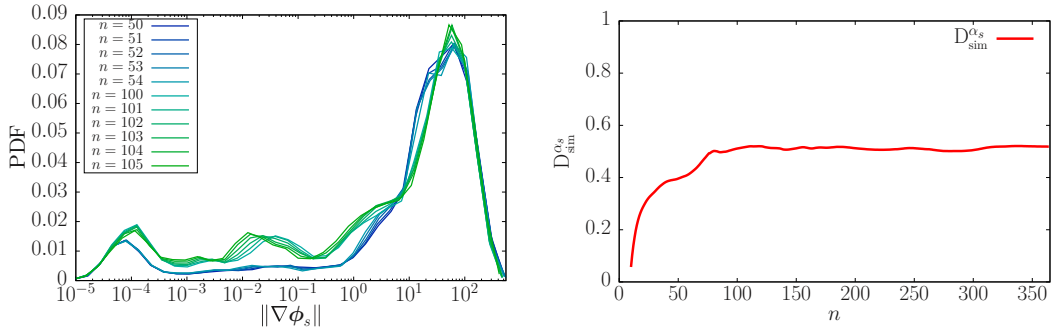

FIG. 4. (a) displays the probability density function (PDF) distribution of $\|\nabla \boldsymbol{\phi}_s\|$ at different time segments in the bubbling FB, where $\|\nabla \boldsymbol{\phi}_s\|$ data are represented on the logarithmic scale after an exponential bin width division. Note that the highest PDF event which corresponds to the gas-filled areas outside the bed, i.e., $\|\nabla \boldsymbol{\phi}_s\| = 0$, is omitted. (b) represents the mean (off-diagonal) most similarity for α_s [Eq. (3)] in the bubbling FB.

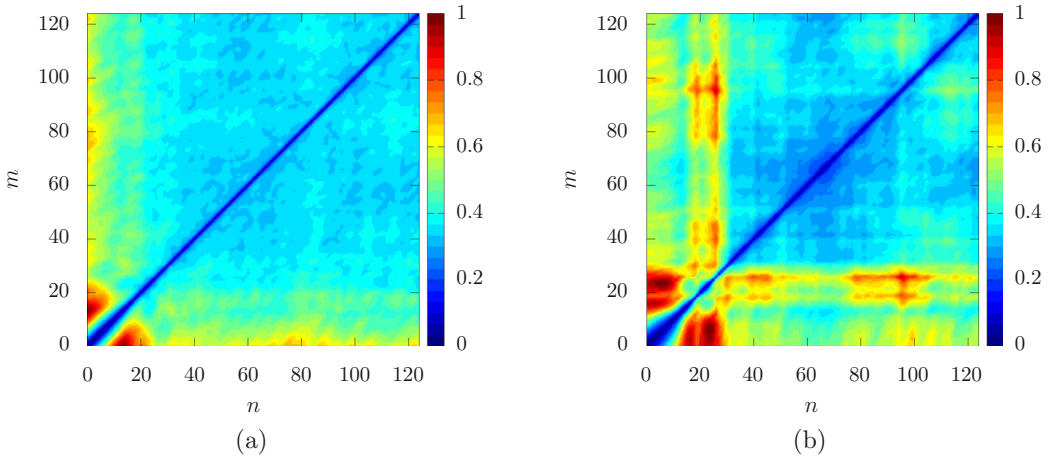

FIG. 5. The dMatrix of the dNorm D^{α_s} in (a) and D^{ϕ_s} in (b) for the turbulent fluidized bed.

any recurrent patterns. This can be seen on the dMatrices with a period that lasts about 30 frames starting from the beginning. Afterwards, the dynamics holds a picture of bubble clusters [Fig. 9(b)] that move randomly in the bulk center and produce a lead dispersion on the solids. The particles, thereby, tend to reside next to the bed sidewalls at heights good far from the perforated bottom plate. By looking at the dMatrices patterns displayed in Figs. 5(a) and 5(b), one cannot recognize any recurrence tendency where the dissimilarity between states (dNorm) is running almost uniform everywhere with an approximate united coloring.

Moreover, the corresponding rVectors, rendered by Figs. 6(a) and 6(b) at $m = 60$ and $m = 65$, respectively, show a very low rProminence, where D^{ϕ_s} does not even unveil any mean. This is principally returned to the dominant turbulent fluctuations and small-scale highly mixed solid structures that correlate the dynamics between states and, therefore, hide any superstructure recurrence. Again, for the current turbulent case this can be supported by performing an identical approach as in the bubbling case in Fig. 4(a). Namely, we plot the PDF charts of $\|\nabla\boldsymbol{\phi}_s\|$ for wide different temporal segments, inside and after the initial disruption stage as manifested in Fig. 7(a). It is worth noting first, this particular distribution presented inside the initial stage where the highest PDF events are pertaining to the low-gradient initial large-scale flow. After this stage, the states present a strong

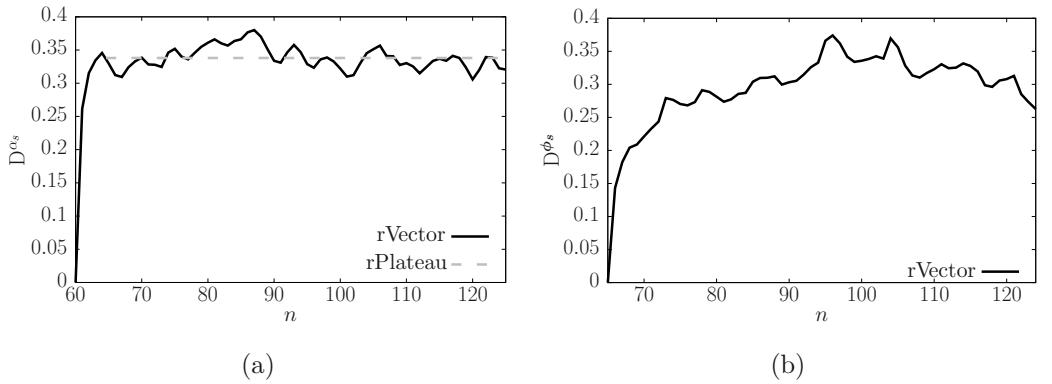

FIG. 6. The rVector profiles taken along the horizontal line $m = 60$ on the dMatrix D^{α_s} in Fig. 5(a) and $m = 65$ on the rMatrix D^{ϕ_s} in Fig. 5(b) in the turbulent fluidized bed.

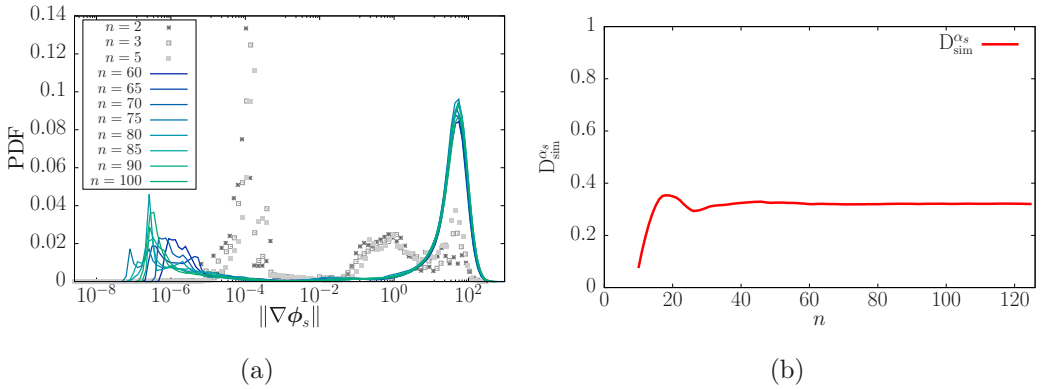

FIG. 7. (a) displays the PDF distribution of $\|\nabla\boldsymbol{\phi}_s\|$ at different time segments in the turbulent FB, where $\|\nabla\boldsymbol{\phi}_s\|$ data are represented on the logarithmic scale after an exponential bin width divisions. (b) represents the mean (off-diagonal) most similarity for α_s [Eq. (3)] in the turbulent FB.

throughout overlapping events clustered at the utmost magnitudes of $\|\nabla\boldsymbol{\phi}_s\|$ (the dominant small-scale mixing structures), which, in turn, confirms the high correlated *local* dynamics in-between the states. It is worth mentioning that the few PDF events that correspond to the lowest values of $\|\nabla\boldsymbol{\phi}_s\|$ in Fig. 7(a), belong to the freeboard dynamics and the bed's surface eruption. Finally, plenty of the turbulent dMatrix sizes are assessed by perceiving the constant plateau of $D^{\alpha_s}_{\text{sim}}$ as shown in Fig. 7(b). In fact, due to the hard solid mixing sustained by the turbulent bubbles, the regime enters in repetition early in time at $n = 40$ and maintains a similarity degree of 0.7 because of the (very close) states correlation.

Further investigations can be conducted in a global sense by focusing on the global similarity of the gradient term $\|\nabla\boldsymbol{\phi}_s\|$ between the states. Put differently, we seek to explore how the underlying small-scale dynamics are recurrent by constructing the dMatrix of $D^{\|\nabla\boldsymbol{\phi}_s\|}$ and render it in Fig. 8(b) (top). It is useful therewith to avoid the early transient states, and the dMatrices building starts at $n = m = 40$. As expected, the figure unveils a kind of smooth feature parallel to the diagonal indicating the close similarity of the small-scale dynamics in-between the states. However, it can be worthwhile, that we decompose these structures in order to certainly clarify where this similarity is coming from. To do so and by looking at the PDF charts in Fig. 7(a), a distinct common threshold can be recognized at the corresponding utmost PDF event. It reads a value of $\|\nabla\boldsymbol{\phi}_s\| = 50$, which reflects the most widespread and dominant structures in correspondence to the high good mixing. Therefore, we build the dMatrices of $D^{\|\nabla\boldsymbol{\phi}_s\|}$ *conditioned* by higher and lower range values than the threshold $\|\nabla\boldsymbol{\phi}_s\| = 50$ and display them in Fig. 8(b) at the middle and bottom, respectively. It is stimulating again to note the different pictures of dMatrices for the two ranges where the extensive-gradient fine structures ($\|\nabla\boldsymbol{\phi}_s\| > 50$) fluctuate significantly in time and gives a high degree of correlated segments [Fig. 8(b) middle]. Note the fine filament structures determined by $\|\nabla\boldsymbol{\phi}_s\| > 50$ in Fig. 8(a) (first right), and how they contribute to the underlying small scales in-between the *large* uniform flow in $\|\boldsymbol{\phi}_s\|$ (first left) and α_s (second left) maps. Differently, the irrelevant low-gradient large structures ($\|\nabla\boldsymbol{\phi}_s\| < 50$) are the main source of $\|\nabla\boldsymbol{\phi}_s\|$ smooth periodicity where its dMatrix, which is shown in Fig. 8(b) (bottom), exposes that kind of parallel-diagonal patterns. See, in this regard, how the structures, determined by $\|\nabla\boldsymbol{\phi}_s\| < 50$ in Fig. 8(a) (second right), constitute the irrelevant coherent uniform flow. However, at the end, it should be admitted that in this turbulent fluidization regime, a hard coupling of the small- and large-scale dynamics is predominantly persistent since the PDF profile around $\|\nabla\boldsymbol{\phi}_s\| = 50$ in Fig. 7(a) is very narrow. This in total yields to the conclusion that disclosing the recurrence properties for such *hardly existing* superstructure in the *pure* turbulent regime is a pipe dream.

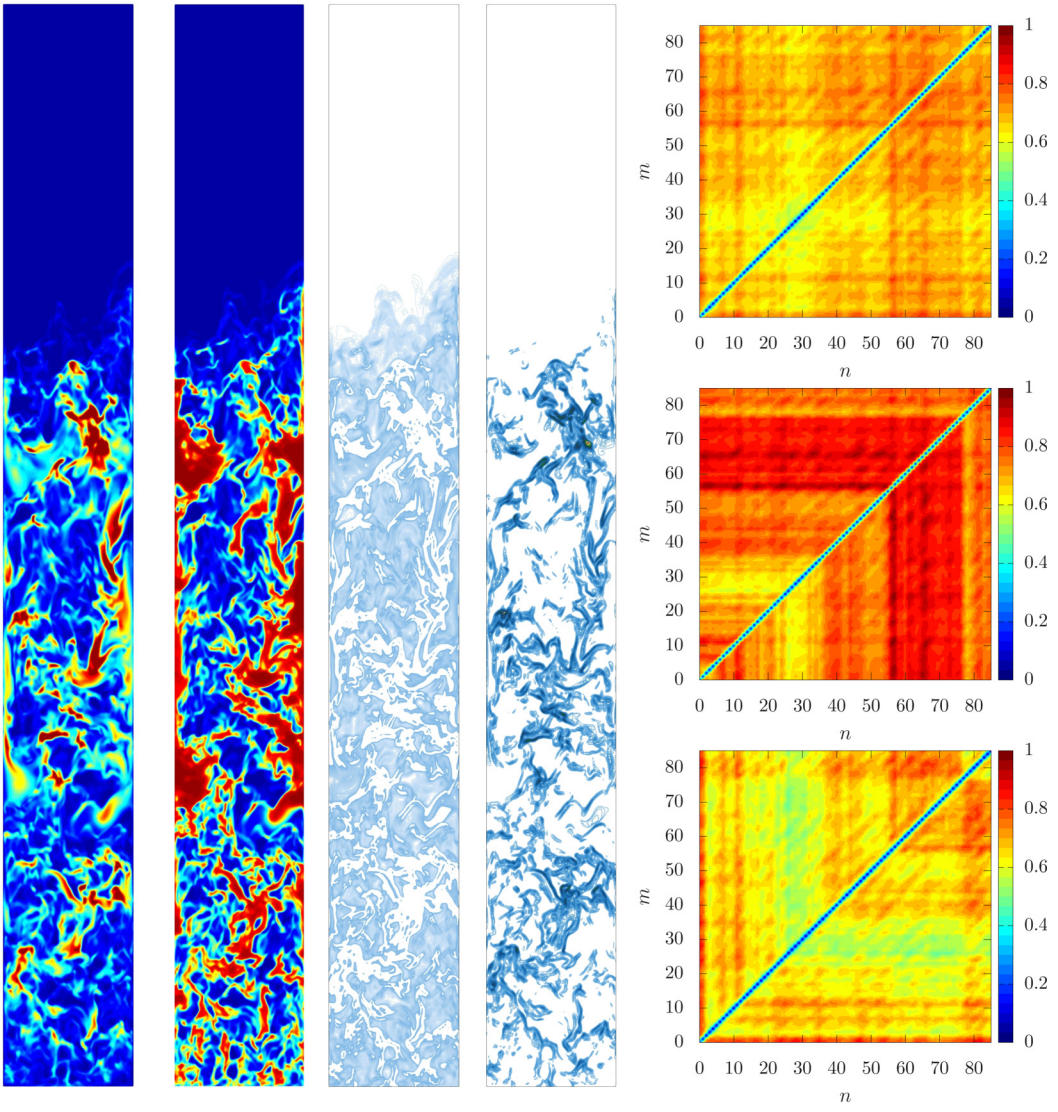

FIG. 8. (a) shows midwidth planes of $\|\boldsymbol{\phi}_s\|$ (first left), α_s (second left), $\|\nabla\boldsymbol{\phi}_s\| > 50$ (first right), and $\|\nabla\boldsymbol{\phi}_s\| < 50$ (second right), taken from the turbulent fluidized bed at state ($n = 125$). (b) depicts the dMatrices of $D^{\|\nabla\boldsymbol{\phi}_s\|}$ when $\|\nabla\boldsymbol{\phi}_s\|$ is not conditioned (top) or conditioned by $\|\nabla\boldsymbol{\phi}_s\| > 50$ (middle) and $\|\nabla\boldsymbol{\phi}_s\| < 50$ (bottom) for the same turbulent FB.

A. Spatial filtering

In order to avoid the high noised mixing and wash out of the rich fluctuation structures, one may employ a spatial filtering. We can apply a spatial filter on the original fields, e.g., α_s and $\boldsymbol{\phi}_s$, which diffuses the superstructure motions by dissipating/eliminating the small scales. To do so, a second-order (Taylor expansion) discrete elliptic differential filter [23],

$$\bar{\varphi}(\boldsymbol{r}, t) = \boldsymbol{\mathcal{F}}\varphi(\boldsymbol{r}, t) = (\mathbf{1} + a^2\nabla^2)\varphi(\boldsymbol{r}, t) \tag{4}$$

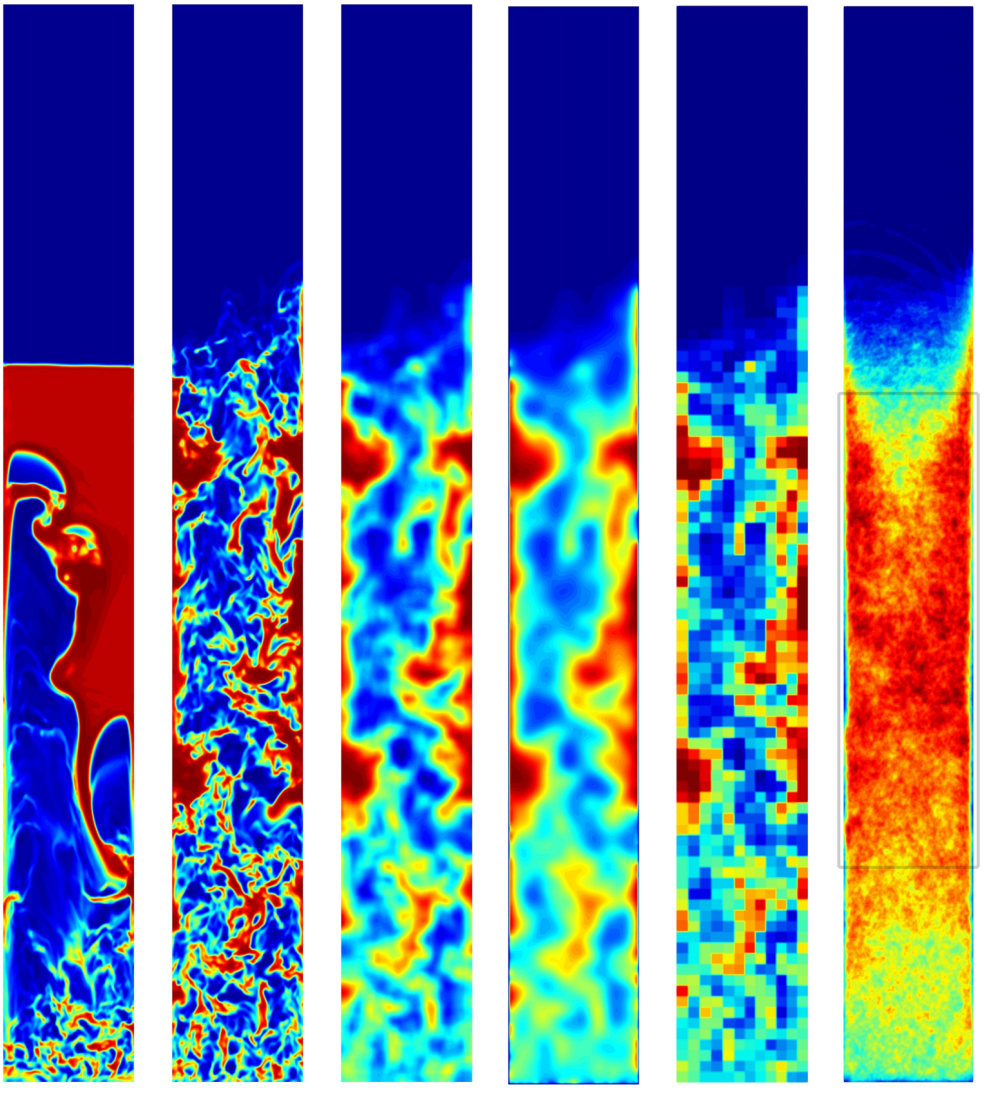

FIG. 9. Midwidth plane of α_s taken from the turbulent fluidized bed: (a) Initial-state $n = 14$. (b) State $n = 125$. (c) Filtered $n = 125$ using box filter $\bar{\Delta} = 12\,\Delta \boldsymbol{r}_i$. (d) Filtered $n = 125$ using elliptic filter $\boldsymbol{\mathcal{F}}^{(128)}$. (e) Filtered $n = 125$ using $10\times$ binning procedure. (f) presents the variance $\langle \alpha_s'^2 \rangle$ as an indicator for the less homogeneous area, i.e., rIsland (the gray line frame).

is used, where $a^2 \leqslant 1/6$. This equation constitutes the general second-order discrete operator of the filters used in the large-eddy simulation, such as box filter (top hat), Gaussian filter, etc. By applying the filter several times $\boldsymbol{\mathcal{F}}^{(i)}$, we can actually broaden the filtering length to get further smoothed structures. Apart from the elliptic filter, we adopt other filters for comparison, such as the box filter that takes the mean value of cells' neighbors, including itself within $\bar{\Delta}$, and the binning procedure which makes the mean for each $\bar{\Delta}$ content and runs block by block.

See, in Fig. 9, first the pure turbulent FB snapshot of α_s in [Fig. 9(b)], and its filtering results using the box filter $\bar{\Delta} = 12\,\Delta \boldsymbol{r}_i$ [Fig. 9(c)], the elliptic filter $\boldsymbol{\mathcal{F}}^{(128)}$ [Fig. 9(d)] and the $10\times$ binning

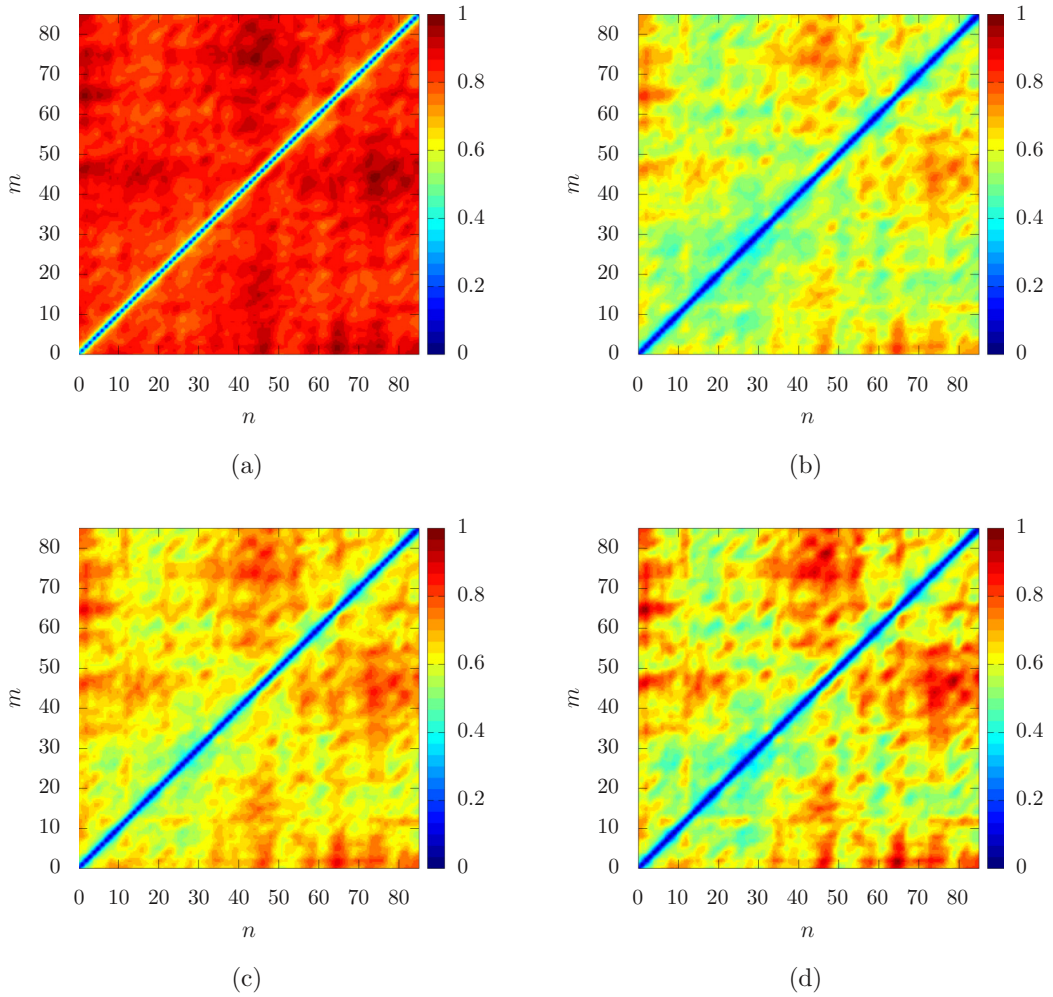

FIG. 10. dMatrices of D^{α_s} in (a) and its outcomes applying filtered fields $D^{\bar{\alpha}_s}$ using the box filter $\bar{\Delta} = 12\,\Delta \boldsymbol{r}_i$ (b), the $10\times$ binning procedure (c), and the elliptic filter $\boldsymbol{\mathcal{F}}^{(128)}$ (d). The normalization maximals, i.e., denominator in Eq. (1) scaled by the volume, are as follows: (a) 0.05, (b) 0.03, (c) 0.03, and (d) 0.016.

procedure [Fig. 9(e)]. One can observe how the uniform structures become diffused and expanded by applying longer lengths of filtering. Building the dMatrices for the filtered $\bar{\alpha}_s$, the picture of the pure turbulent α_s dMatrix turns from strong dissimilarity reflected in almost uniform red in Fig. 10(a) to an enhanced appearance of blue parallel-diagonal segments in Figs. 10(b)–10(d).

Basically, the filtering approach reduces the magnitude of dissimilarity to unveil the coherent uniform-flow superstructure recurrence. It highly discloses the large-scale fingerprints on dMatrices and gives better visualization for the recurrence process. Eventually, this filtering approach can be very helpful in trailing the mean solution which is usually the most interesting feature in turbulent flows. Looking at the $D^{\bar{\alpha}_s}$ dMatrices in Fig. 10, one can see the better recurrence tendency obtained using longer filter lengths, such as the elliptic $\boldsymbol{\mathcal{F}}^{(128)}$ [Fig. 10(d)] and $10\times$ binning [Fig. 10(c)] in comparison with the box filter $\bar{\Delta} = 12\,\Delta \boldsymbol{r}_i$ [Fig. 10(b)].

In a direct assessment way, the filtering performance can be fundamentally revealed by investigating the corresponding rVectors and rProminence. Hence, we extract rVectors in Fig. 10 at $m = 20$ and plot them in Fig. 12. Therein, each profile is normalized by its own rPlateau in order

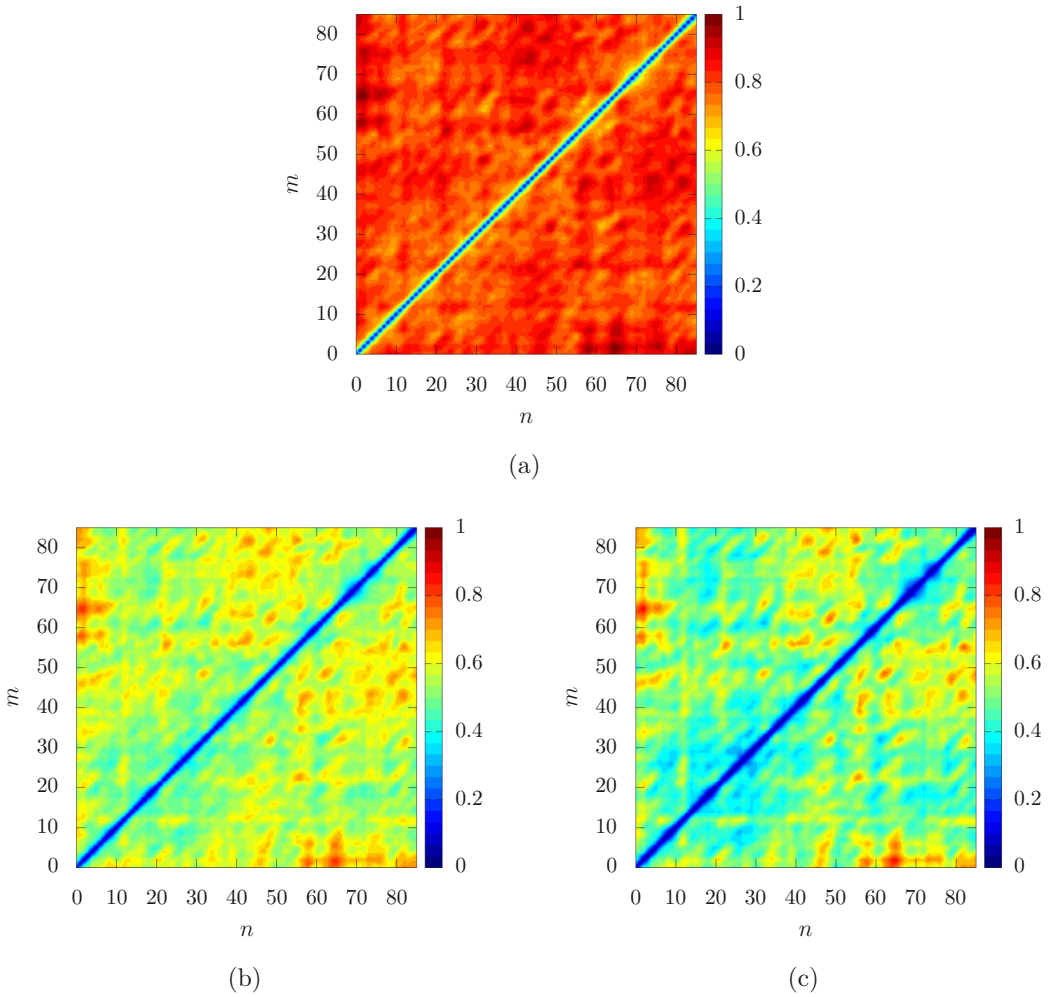

FIG. 11. dMatrices of the rIsland displayed in Fig. 9(f) (gray line frame) for D^{α_s} in (a) and its outcomes applying filtered fields $D^{\bar{\alpha}_s}$, the 10× binning procedure (b), and the elliptic filter $\mathcal{F}^{(128)}$ (c). The normalization maximals, i.e., denominator in Eq. (1) scaled by the volume, are as follows: (a) 0.035, (b) 0.025, and (c) 0.014.

to be comparable among each other. Hence, by looking inside, the filtered approaches do show an important rProminence in comparison with the no filtering, and this variance (rProminence grade) becomes larger at wider filter lengths. On the other hand, it is interesting to note that the filters do not change the structure of the dMatrix. They only expose the recurrent properties hidden by the turbulent fluctuations to be more visible.

Further enhancement on recurrence featuring can be as well by focusing on those visually less mixing areas. For instance, if we look at the pure turbulent snapshot in Fig. 9(b), we can note that the lower part next to the inlet is homogeneously fluidized and well mixed. This may be verified by computing the variance of α_s as

$$\left\langle \alpha_s'^2 \right\rangle = \langle \alpha_s \alpha_s \rangle - \langle \alpha_s \rangle \langle \alpha_s \rangle, \tag{5}$$

where its highest magnitude corresponds to the less homogeneous areas. Consistent to our view, the map of $\langle \alpha_s'^2 \rangle$, depicted in Fig. 9(f), shows higher values (red regions) far above the inlet, whereas the lowest ones (green towards blue) reside next to the inlet and outside the bed. This can lead us

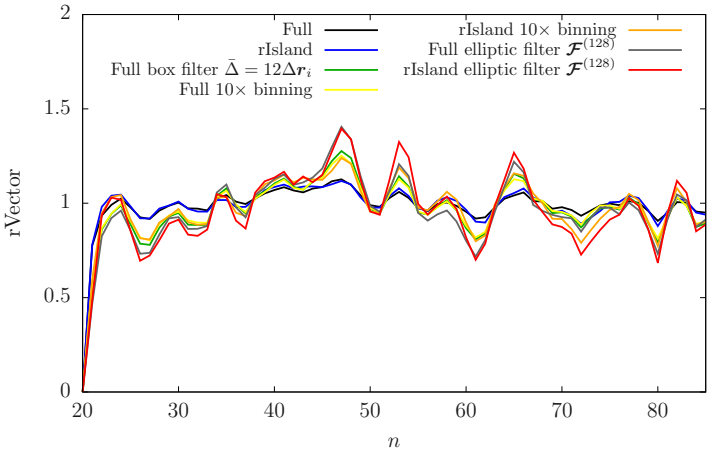

FIG. 12. The rVector profiles taken along the horizontal line $m = 20$ on the dMatrices in Figs. 10 and 11 and normalized by its own rPlateau.

to a kind of intensive-recurrent areas identification, called recurrence islands (rIsland), which are detached from the rest of the domain, i.e., the background sea. The rIslands in our case can then be detected following the lowest mixing grade and the utmost values of $\langle \alpha_s'^2 \rangle$ about a determined threshold. Since our study is generic and aiming to only analyze recurrence properties, we simply choose the part of the domain marked by the gray line frame in Fig. 9(f) as an rIsland. Therewith, the dMatrices of D^{α_s} belong to that part and their filtered outcomes (using elliptic $\mathcal{F}^{(128)}$ and 10× binning) are built and rendered in Fig. 11.

It is worth noting now the enhanced appearance of more recurrent runs with lower dissimilarity, particularly, in the elliptic filter $\mathcal{F}^{(128)}$ case. This can be more visible in the corresponding rVector profiles plotted in Fig. 12 together with the previous entire domain results. Similar to the others, the rIsland rVectors are also normalized by its rPlateau and reveal the best recurrence indicators with the highest rProminence utilizing the elliptic filter $\mathcal{F}^{(128)}$.

To conclude, applying an *a posteriori* procedure that removes *spatially* the rich fluctuation structures, such as the filtering approach, is an essential require to expose the recurrence properties in turbulent fluidization.

B. Turbulence modeling

On the top of the previous findings, the key ingredient of disclosing the turbulent fluidization recurrence rises from reducing the fluctuation effect of the interphase small scales. So, employing a turbulence model can as well comply with that requirement. Namely, a turbulence model imposes spatial filtering with a direct resolving to the more energetic large-scale dynamics, whereas the subgrid-scale rich fluctuation turbulence is modeled. Following this concept, we simulate the same turbulent fluidized bed using a filtered two-fluid model where the unresolved terms are closed by employing an approximate deconvolution model (ADM-TFM) [22]. After storing the series sequences of (modeled) fields, similar recurrence procedures as depicted in Fig. 5, but discarding the initial stage, are pictured in Figs. 13(a) top (solid flux) and middle (solid volume fraction). It can be clearly observed the appearing of blue patterns parallel to the diagonal which exposes the good recurrence in both coarse-grained fields dMatrices. For instance, if we picture two states of a low dNorm value on the $\bar{\alpha}_s$ dMatrix [Fig. 13(a) (middle)], e.g., $D^{\bar{\alpha}_s}(42, 3)$ (black circle), one can note the remarkable similarity shown in Fig. 13(b). The interesting issue is that the coarse-grained (ADM-TFM) recurrence properties are very comparable to the spatial filtering approach, particularly, the box filter $\bar{\Delta} = 12\,\Delta r_i$ or 10× binning procedure (which render almost the same

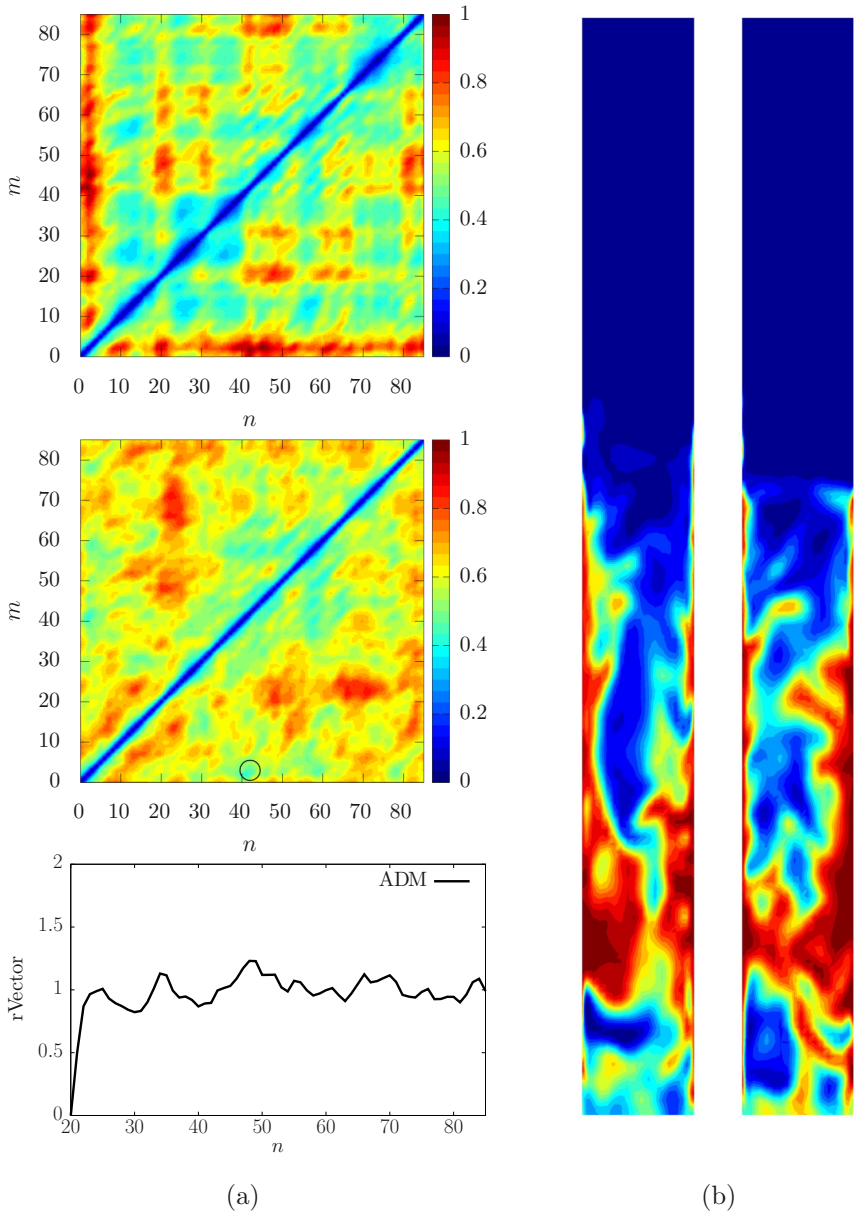

FIG. 13. (a) represents the dMatrices of $D^{\bar{\phi}_s}$ (top), $D^{\bar{\alpha}_s}$ (middle), and the rVector along $m = 20$ on $D^{\bar{\alpha}_s}$ dMatrix, normalized by its rPlateau (bottom), for the coarse-grained (ADM-TFM) turbulent fluidized bed. (b) displays midwidth planes of one recurrent point $D^{\bar{\alpha}_s}(42, 3)$ (black circle) in (a) (middle). The normalization maximals, i.e., denominator in Eq. (1) scaled by the volume, are as follows: (a) top 0.07 and (a) middle 0.035.

grid size as ADM-TFM). Meaning that, if we plot the rVector at $m = 20$ on $D^{\bar{\alpha}_s}$ dMatrix [Fig. 13(a) (middle)], normalized by its rPlateau, the resultant rProminence as shown in Fig. 13(a) (bottom), is almost the same in Fig. 12 (full box filter $\bar{\Delta} = 12\,\Delta \boldsymbol{r}_i$ and full $10\times$ binning). Hence, similar to the spatial filtering, applying a turbulence modeling, can as well disclose the recurrent superstructure properties in turbulent fluidization. It differs than the spatial filtering in the recurrence frequency because of the systems nonlinearity but leading to the same similarity/dissimilarity magnitudes.

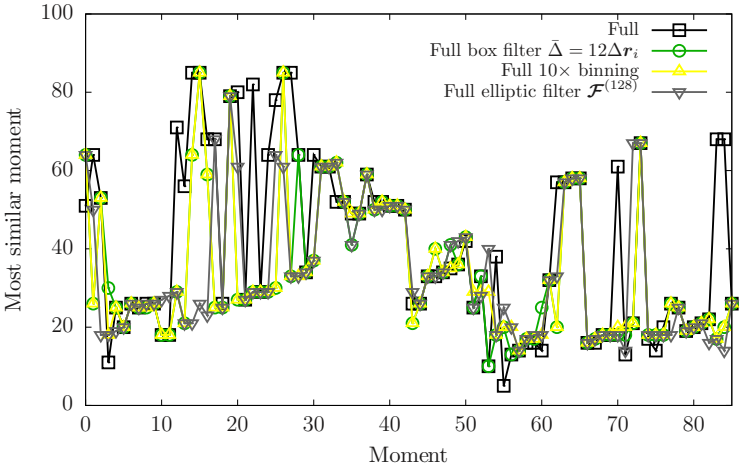

FIG. 14. jVectors extracted from the dMatrices in Fig. 10.

C. Implications to rCFD

The recurrence CFD process (rProcess) implicates the generation of a recurrence path (rPath) on the base of rMatrix/dMatrix, which extends a passive evolution far beyond the recording time span [2]. The rPath is extracted randomly by choosing a temporal interval of segments inside the rMatrix/dMatrix sizes and jump to the most similar moment at the end of this interval. In order to check the influence of spatial filtering on this jumping process, and, thus, the rProcess, we consider an array of the minimal dNorms on the dMatrix in corresponding to each m moment. This array holds the most similar moment index of every moment m, e.g., $array[5] = 20$ means that the moment 20 is the most similar to 5 with the lowest dNorm. If we call this array as a jump vector (jVector), its representations are displayed in Fig. 14 for the pure turbulent case and the different filters, extracted from the dMatrices in Fig. 10. One can note that, although the filtering approach does not significantly change the structures of the dMatrices (as seen in Figs. 10 and 12), however, on the level of segments, it can modify the jVector leading to jump towards different moments. This modification can be more observant at wider filter lengths (elliptic filter $\mathcal{F}^{(128)}$) when the recurrent segments of high rProminence can grow and run longer. A proper decision on the filter length extent required to disclose the large-scale recurrence properties can be obtained using the two-point correlation. To do so, we investigate the correlation of α_s^c vertical midlength plane with its neighboring towards the walls and using the formula,

$$\mathrm{Corr} = \frac{\langle \alpha_s'(\boldsymbol{r}_i^c)\alpha_s'(\boldsymbol{r}_i^c + \Delta\boldsymbol{r}_0)\rangle}{\langle \alpha_s'(\boldsymbol{r}_i^c)\rangle}. \tag{6}$$

It measures the correlated fluctuations of α_s starting from the vertical center-length points towards the walls. By considering multiple heights {0.05:0.8}, the resultant profiles are represented in Fig. 15 to show a separation scale after about $\Delta\boldsymbol{r}_0 \sim 0.01$. This length, in fact, consists with the filter size of the coarse-grained ADM-TFM (see Table I). Therefore, one can conclude that using the box filter $\bar{\Delta} = 12\,\Delta\boldsymbol{r}_i$ or 10× binning procedure, which render almost the same grid size and rProminence as ADM-TFM is the utmost appropriate approach for rCFD application.

In the end, this spatial filtering falls in the advantage of being solely a posterior postprocessing procedure analyzing the pure turbulent database, whereas the turbulence modeling is a new simulation. Notably, the method of proper orthogonal decomposition (POD) [24] constitutes an alternative approach to extract coherent superstructures with pronounced recurrences [25]. It has been employed for the analysis of recurring events in turbulent flows [10] and, more recently, in

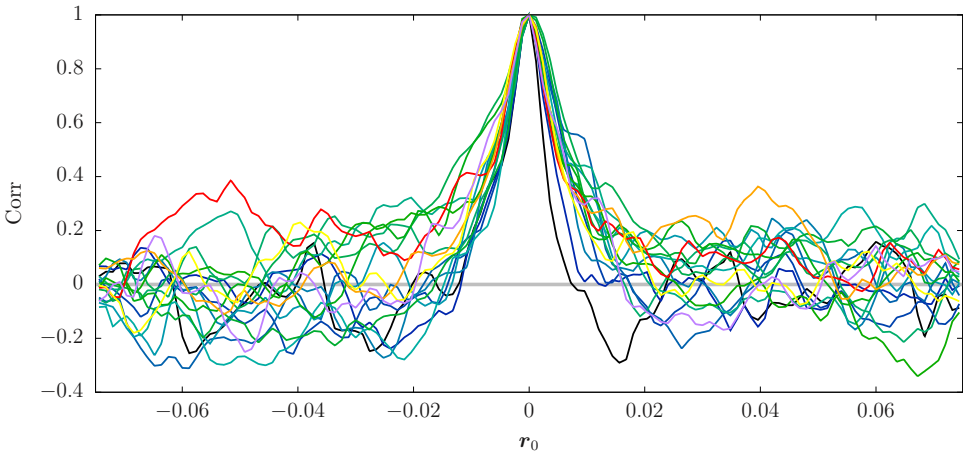

FIG. 15. Two-point correlation profiles of α_s starting from the midlength plane towards the walls and extracted at different heights {0.05:0.8} inside the turbulent FB.

the framework of rCFD for the fast modeling of species transport in a confined turbulent jet [26]. In the latter case, a reconstruction of the coherent fields from a small number of low-order modes (maximum kinetic-energy content) revealed significant recurrent patterns in the dMatrix. Eventually, this led to a similar picture as the results from spatial filtering presented in this paper. However, we stress that filtering is numerically cheaper than solving the eigenvalue problem of POD and less complicated to set up but requires an *a priori* decision on the filter length.

IV. CONCLUDING REMARKS

In this paper, we give a short review of inspecting the recurrence properties for bubbling and turbulent fluidized bed reactors. In principle, the recurrence/distance norms and recurrence/distance matrices are considered to judge the recurrent phenomena. It is found that the full-resolved turbulent regime exposes no recurrence tendency within the observation time in contrast to the bubbling fluidization regime. It is argued thereabouts, that the highly mixed (fluctuated and dominant) interphasic small scales make the states meaningfully correlated and absentee its similarity. Because of the considerable mixing presented in the turbulent fluidization, the small and large scales are strongly coupled to obtain a significant value of $\|\nabla \boldsymbol{\phi}_s\|$. This is then showed a kind of smooth *underlying* recurrence owing to the correlation. Thus, the uniform superstructures are hardly identified in the turbulent regime because of the hard mixing, and a short-term history of turbulent dynamics is sufficiently representative. As a remedy, a posterior spatial filtering on the fields is applied in order to wash out the fluctuation effects. More precisely, different filters with various lengths are employed and shown a good disclosure of the large-scale dynamics with recurrent fingerprints on the distance matrices. The filtering approach arises the recurrence prominence without changing the behavior of the system. We stress that even though filtering increases the prominence of a distance matrix and reveals otherwise hidden recurrences, it does not change intrinsic dynamic properties. Although filtered fields look differently than the unfiltered ones, the contained information is not lost but reorganized. As discussed in Ref. [27], the correlation dimension and the prediction time of a gas-solid flow show hardly any dependence of the length of a box filter.

Another focus on the recurrent dynamics is realized by decomposing the domain to intensive recurrent islands and the stable (well-mixed) background sea. Namely, following the variance field of α_s, the highest values correspond to the less homogeneous areas which presented a prominent degree of recurrence. Its distance matrices have shown an enhanced appearance of recurrence with the lowest dissimilarity using the elliptic filter $\mathcal{F}^{(128)}$.

On the other hand, a filtered TFM in which the unresolved terms are closed by employing an approximate deconvolution model (ADM-TFM) [22] is used to compare the recurrence properties of the turbulent fluidization case. As a result, the recurrence prominence offered by ADM-TFM have revealed a very comparable aspect to the spatial filtering approach (of the same level grid size) using the box filter $\bar{\Delta} = 12\,\Delta \boldsymbol{r}_i$, or the $10\times$ binning procedure. At the end, these latter have been demonstrated as the appropriate filter length extents needed to disclose the large-scale recurrence and rCFD application for the studied turbulent fluidization case.

ACKNOWLEDGMENTS

Financial support by the Austrian Federal Ministry for Digital and Economic Affairs and the National Foundation for Research, Technology and Development is gratefully acknowledged. We further want to acknowledge the funding support of K1-MET GmbH Metallurgical Competence Center. The Research Programme of the K1-MET Competence Center is supported by Competence Center for Excellent Technologies (COMET), the Austrian Programme for Competence Centers. COMET is funded by the Federal Ministry for Transport, Innovation and Technology, the Federal Ministry for Digital and Economic Affairs, and the provinces of Upper Austria,Tyrol, and Styria.

[1] J. Wang, Continuum theory for dense gas-solid flow: A state-of-the-art review, Chem. Eng. Sci. **215**, 115428 (2020).
[2] T. Lichtenegger and S. Pirker, Recurrence CFD–a novel approach to simulate multiphase flows with strongly separated time scales, Chem. Eng. Sci. **153**, 394 (2016).
[3] J. P. Eckmann, S. O. Kamphorst, and D. Ruelle, Recurrence plots of dynamical systems, Europhys. Lett. **4**, 973 (1987).
[4] N. Marwan, M. C. Romano, M. Thiel, and J. Kurths, Recurrence plots for the analysis of complex systems, Phys. Rep. **438**, 237 (2007).
[5] M. Tahmasebpour, R. Zarghami, R. Sotudeh-Gharebagh, and N. Mostoufi, Characterization of various structures in gas-solid fluidized beds by recurrence quantification analysis, Particuology **11**, 647 (2013).
[6] B. Babaei, R. Zarghami, H. Sedighikamal, R. Sotudeh-Gharebagh, and N. Mostoufi, Investigating the hydrodynamics of gas–solid bubbling fluidization using recurrence plot, Adv. Powder Technol. **23**, 380 (2012).
[7] S. Pirker and T. Lichtenegger, Efficient time-extrapolation of single-and multiphase simulations by transport based recurrence CFD (rCFD), Chem. Eng. Sci. **188**, 65 (2018).
[8] T. Lichtenegger, Local and global recurrence in dynamic gas-solid flows, Int. J. Multiphase Flow **106**, 125 (2018).
[9] B. Goswami, A brief introduction to nonlinear time series analysis and recurrence plots, Vibration **2**, 332 (2019).
[10] S. Lardeau, F. Tessicini, and M. A. Leschziner, Analysis of cyclic events in turbulent flows using recurrence plots, J. Turbul. **11**, N16 (2010).
[11] K. Mulleners and M. Rütten, Analysis of intermittent trailing-edge vortex shedding using recurrence plots, AIAA J. **56**, 571 (2018).
[12] A. D. Fragkou, T. E. Karakasidis, and I. E. Sarris, Recurrence quantification analysis of MHD turbulent channel flow, Physica A **531**, 121741 (2019).
[13] Y. Hirata, Recurrence plots for characterizing random dynamical systems, Commun. Nonlinear Sci. Numer. Simul. **94**, 105552 (2021).
[14] R. Zarghami, F. Sharifi, and N. Mostoufi, Investigating the hydrodynamics of high temperature fluidized bed by recurrence plot, Exp. Therm Fluid Sci. **83**, 88 (2017).
[15] M. F. Llop, N. Gascons, and F. X. Llauró, Recurrence plots to characterize gas-solid fluidization regimes, Int. J. Multiphase Flow **73**, 43 (2015).

[16] M. Tahmasebpoor, R. Zarghami, R. Sotudeh-Gharebagh, J. R. van Ommen, and N. Mostoufi, Dynamic analysis of the scale-up of fluidized beds, Adv. Powder Technol. **28**, 2621 (2017).
[17] T. Lichtenegger, E. A. J. F. Peters, J. A. M. Kuipers, and S. Pirker, A recurrence CFD study of heat transfer in a fluidized bed, Chem. Eng. Sci. **172**, 310 (2017).
[18] T. Lichtenegger, P. Kieckhefen, S. Heinrich, and S. Pirker, Dynamics and long-time behavior of gas-solid flows on recurrent-transient backgrounds, Chem. Eng. J. **364**, 562 (2019).
[19] F. Dabbagh, S. Pirker, and S. Schneiderbauer, On the fast modeling of species transport in fluidized beds using recurrence computational fluid dynamics, AIChE J. **66**, e16931 (2020).
[20] B. G. M. van Wachem, J. C. Schouten, C. M. van den Bleek, R. Krishna, and J. L. Sinclair, Comparative analysis of CFD models of dense gas-solid systems, AIChE J. **47**, 1035 (2001).
[21] A. Bakshi, A. F. Ghoniem, and C. Altantzis, Mixing dynamics in bubbling fluidized beds, AIChE J. **63**, 4316 (2017).
[22] S. Schneiderbauer and M. Saeedipour, Numerical simulation of turbulent gas-solid flow using an approximate deconvolution model, Int. J. Multiphase Flow **114**, 287 (2019).
[23] P. Sagaut and R. Grohens, Discrete filters for large eddy simulation, Int. J. Numer. Methods Fluids **31**, 1195 (1999).
[24] G. Berkooz, P. Holmes, and J. L. Lumley, The proper orthogonal decomposition in the analysis of turbulent flows, Annu. Rev. Fluid Mech. **25**, 539 (1993).
[25] L. Sirovich, Turbulence and the dynamics of coherent structures. I. Coherent structures., Q. Appl. Math. **45**, 561 (1987).
[26] S. Abbasi, S. Puttinger, S. Pirker, and T. Lichtenegger, Recurrence analysis and time extrapolation of a confined turbulent jet using modal decomposition, Phys. Fluids **32**, 075115 (2020).
[27] T. Lichtenegger and T. Miethlinger, On the connection between lagrangian and eulerian metrics for recurrent particulate flows, Phys. Fluids **32**, 113308 (2020).